The Astrophysical Journal, 976:113 (9pp), 2024 November 20 https://doi.org/10.3847/1538-4357/ad81f4

The Effect of Anisotropic Energy Injection on the Ejecta Emission

Yu-Fei Li[1], Da-Bin Lin[1], Li Zhou[1], Jia Ren[2], Zhi-Lin Chen[1], and En-Wei Liang[1]
[1] Guangxi Key Laboratory for Relativistic Astrophysics, School of Physical Science and Technology, Guangxi University, Nanning 530004, People's Republic of China; lindabin@gxu.edu.cn
[2] School of Astronomy and Space Science, Nanjing University, Nanjing 210023, People's Republic of China
Received 2023 July 3; revised 2024 September 27; accepted 2024 September 29; published 2024 November 15

Abstract

A rapidly rotating magnetar has long been assumed to inject energy into the ejecta through isotropic output energy in previous works. However, the output energy of a magnetar is anisotropic and a jet is generally presented in the rotational direction of a magnetar. In this paper, we present a consistent model of the energy injection from a magnetar, considering both the anisotropic magnetic dipole radiation and the jet's ingredient (i.e., the late jet mentioned refers to the beamed magnetars wind). In the situation that the energy injection into the ejecta presents a significant effect on the ejecta's emission, two facts are obtained. (1) For an observer in the equatorial direction, there is no significant difference between the light curves of the ejecta's emission based on the consistent model and those obtained in previous works (i.e., based on the isotropic energy injection). (2) For an on jet-axis observer, however, the difference is significant, especially in the optical/U-band. If the jet is not present in the system, the rise of the optical/U-band light-curve is actually steeper than that in previous works because the output energy of the anisotropic magnetic dipole radiation is mainly in the equatorial direction. If the jet is present in the system, a bump from the cocoon (i.e., the late jet launch is expected to shock and heat-up the ejecta) may only appear in the optical/U-band light curve for a quasi-isotropic ejecta. Our results reveal that the anisotropic energy output of the magnetic dipole radiation and the jet's ingredient should be well considered in modeling the ejecta emission by considering the energy injection from a magnetar. In addition, the optical/U-band light-curve may disclose the central engine of the burst.

Unified Astronomy Thesaurus concepts: Gamma-ray bursts (629)

1. Introduction

GW170817 is a gravitational wave (GW) event that was detected by Advanced LIGO and Advanced Virgo (B. P. Abbott et al. 2017a). In 1.7 s after the merger, a burst of gamma-rays (GRB 170817A) was detected by the Fermi Gamma-ray Burst Monitor (Fermi-GBM; B. P. Abbott et al. 2017b; A. Goldstein et al. 2017) and INTEGRAL SPI-ACS (the anti-coincidence system of spectrometer SPI on the International Gamma-Ray Astrophysics Laboratory; V. Savchenko et al. 2017). Subsequently, the optical counterpart (AT 2017gfo) was also detected, confirming the theoretical prediction of kilonova phenomena driven by radioactive decay of heavy elements in the r-process. The brightest electromagnetic (EM) emission during the compact binary mergers is probably short-duration gamma-ray bursts (sGRBs; D. B. Fox et al. 2005; N. Gehrels & C. L. Sarazin 2005; F. J. Virgili et al. 2011; W. Fong et al. 2013). However, since they are usually beamed into a small opening angle (e.g., D. N. Burrows et al. 2006; M. De Pasquale et al. 2010), most GW bursts would not be detected together with sGRBs (e.g., B. D. Metzger & E. Berger 2012). Recent works have shown that the remnant compact object of GW170817 may be a stable long-lived magnetized neutron star (NS). In this situation, the magnetic dipole radiation of the magnetized NS can provide additional energy injected into the ejecta. This process would significantly increase the luminosity of the kilonova (Y.-Z. Fan et al. 2013; Y.-W. Yu et al. 2013; H. Gao et al. 2015). With an additional energy injection from the merger central region, the ejecta mass required to explain the observations can be somewhat smaller than that in the multicomponent model (S.-Z. Li et al. 2018; Y.-W. Yu et al. 2018). In fact, the ejecta with energy injection from a magnetized NS has been studied in explaining the observations of AT 2017gfo (T. Matsumoto et al. 2018; B. D. Metzger et al. 2018; Y.-W. Yu et al. 2018).

In the process of NS–NS/black hole (BH) merger, a significant mass (the typical mass of the ejecta is in the range $M_{\rm ej}\sim 10^{-4}$–$10^{-2}\,M_{\odot}$) is ejected in these cataclysmic events and expands outward at a velocity of $\sim 0.2c$ (M. Shibata 1999; K. Hotokezaka et al. 2013; D. Radice et al. 2018; H. Hamidani & K. Ioka 2021). These catastrophic events are usually accompanied by the launch of relativistic jet from the central region. The GRB's prompt emission is produced by emission from this jet in the line of sight (M. Ruderman 1975). The jet is initially surrounded by the dense ejecta and it had to propagate through this dense ejecta to produce the observed GRB prompt emission (H. Hamidani et al. 2024). Relativistic jets transport a large amount of energy to great distances from the source and they also interact with the ambient medium (H. Hamidani et al. 2024). The jet propagates by pushing the matter in front of it, leading to the formation of a forward shock and a reverse shock at the jet's front that are separated by a contact discontinuity, this structure is referred to as the jet's head (see Figure 1 in O. Bromberg et al. 2011). Matter that enters the head through the shocks is heated and flows sideways because its pressure is higher than that of the surrounding matter. This leads to the formation of a pressured cocoon around the jet (see Figure 1 in O. Bromberg et al. 2011). During the propagation of the relativistic jet in the pre-ejected mass, the jet continuously injects energy into the expansive dynamic ejecta through the jet head. Hence, the jet's significant energy budget is another

crucial factor to consider in NS mergers (M. M. Kasliwal et al. 2017; E. Nakar & T. Piran 2017; O. Gottlieb et al. 2018). However, the additional energy injection into the ejecta from a relativistic jet during the NS–NS/BH merging process has been rarely considered or even ignored in previous works.

After the prompt phase, interaction of the prompt-jet with the circumstellar medium produces a softer emission, from X-ray to radio, which is called the "afterglow" (R. Sari et al. 1998). In addition, a rapidly rotating magnetar has been shown to be the central engine of some gamma-ray bursts (GRBs), particularly the internal plateau feature of the X-ray afterglow (Z. G. Dai & T. Lu 1998; B. Zhang & P. Mészáros 2001). These observed phases usually show a luminosity curve of flat or shallow temporal behavior, which implies the need for additional energy injection. Although it has been proposed that injecting energy into the forward shock of deceleration could explain this phenomenon (J. A. Nousek et al. 2006; A. Panaitescu et al. 2006; B. Zhang et al. 2006), this cannot explain everything, especially when these phases are followed by a sharp decay (E.-W. Liang et al. 2007; E. Troja et al. 2007). As a result, explaining these phases with afterglow modeling is challenging and their origin has generally been attributed to a late central engine. Recent observations of GRB 211211A (long GRBs but with potential kilonova candidate) show evidence of late emission in the form of a soft tail (J. C. Rastinejad et al. 2022; E. Troja et al. 2022; J. Yang et al. 2022). Hence, in BNS mergers, after the prompt phase, late engine activity is expected to continue in most cases. The specific details of this late engine activity are still unclear, but the flat temporal behavior of the observed luminosity during these late plateau phases requires extra energy. Based on these arguments, the late emission phases are often interpreted as significant indicators of jet outflows resulting from late engine activity (K. Ioka et al. 2005; S. Kisaka & K. Ioka 2015; O. Gottlieb et al. 2023). Therefore, late jet launch is expected to shock and heat-up the ejecta, producing a late cocoon at a much larger radius (than in the prompt-jet case; H. Hamidani et al. 2024).

The NS–NS merger may leave behind a stable millisecond magnetar, which would continuously power the merger ejecta. B. Zhang (2013) proposed that magnetar wind would undergo magnetic dissipation and power a bright X-ray afterglow emission. In addition, a large fraction of the magnetar's wind energy would be used to heat up and push the neutron-rich ejecta to produce a bright "mergernova" (Y.-W. Yu et al. 2013; B. D. Metzger & A. L. Piro 2014; H. Gao et al. 2015, 2017). In previous works, for the convenience of modeling, it is often simply assumed that the simplest form of pulsar energy output can be approximated as nearly isotropic or spherically symmetric pulsar wind (Y.-W. Yu et al. 2013; H. Gao et al. 2015; H. Sun et al. 2017). However, previous discoveries of the intriguing "jet torus" structures in the Crab Nebula and other pulsar nebulae prompted calls for re-examination of the early spherically symmetric magnetohydrodynamic (MHD) model theory of weakly magnetized pulsar winds (e.g., isotropic pulsar wind; J. J. Hester et al. 1995, 2002; M. C. Weisskopf et al. 2000; B. M. Gaensler et al. 2001, 2002; D. J. Helfand et al. 2001; G. G. Pavlov et al. 2001; F. J. Lu et al. 2002; S. S. Komissarov & Y. E. Lyubarsky 2003). Thus, this magnetar wind is nonspherical (anisotropic pulsar wind), which may explain the origin of the "X-ray torus" (also "jet torus"; S. V. Bogovalov & D. V. Khangoulian 2002; Y. E. Lyubarsky 2002). B. Margalit et al. (2018) proposed that the magnetar dissipates a portion of the spin drop power through the reconnection of the striated equatorial winds mechanism, by which the magnetar can power both the relativistic jet and the ejecta. This mechanism can be used naturally to inject jet and magnetar wind energy into the merger ejecta. Recently, Y. Wang et al. (2024) employed special relativity MHD simulations to investigate the wind injection process from a magnetar central engine. They mainly explore the dynamics and energy distribution within the system and found that, if implemented, isotropic energy injection requires a significantly small α (which indicates the collimation of the magnetar wind energy injection) that necessitates either an ultrarelativistic expanding magnetar wind nebular (MWN) or an extremely low magnetization MWN, both of which are challenging to attain in sGRBs.

This paper is based on late jet launch and propagation through BNS merger ejecta at later times (H. Hamidani et al. 2024), we propose a model of the anisotropic pulsar wind and structured jet to provide energy for neutron-rich merger ejecta. We investigate the emission properties of a mergernova driven by anisotropic energy in a magnetar that simultaneously powers a relativistic jet and pulsar wind. This paper is organized as follows. The model, i.e., anisotropic pulsar wind and structured jet provide energy for neutron-rich merger ejecta, is presented in Section 2. The results, i.e., the effects of the jet and magnetar wind anisotropic energy injection on the ejecta emission, are presented in Section 3. The conclusion and discussions are presented in Section 4.

2. Model

An NS–NS merger may leave behind a stable or supermassive millisecond magnetar. The newborn magnetar would release a lot of energy through pulsar wind to power the ejecta. Thus, the continuous energy injection from the magnetar is the most popular source of extra energy for a kilonova. In previous works (e.g., Y.-W. Yu et al. 2013; H. Gao et al. 2015; H. Sun et al. 2017), an isotropic energy injection from a magnetar into the ejecta is generally assumed. However, the output energy of a magnetar is anisotropic and a jet is generally presented in the rotational direction of the magnetar (e.g., S. V. Bogovalov & D. V. Khangoulian 2002; Y. E. Lyubarsky 2002; E. M. Churazov et al. 2024; Y. Wang et al. 2024). During the jet's propagation, a shocked "head" often appears at its front and the jet deposits the energy to a cocoon (O. Bromberg et al. 2011). After the prompt phase, engine activity (and jet propagation) is considered to continue to much later times. Since the prompt jet is shut off at the end of the prompt phase, it takes some time for the central engine to launch the late jet (H. Hamidani & K. Ioka 2023a). This allows the ejecta to redistribute, closing off the path (i.e., hole) created by the prompt jet (S. Fujibayashi et al. 2020). The late jet is expected to propagate through the ejecta in a manner similar the prompt jet, rather than simply through the path of the prompt in the polar direction (H. Hamidani et al. 2024). Here, we refer to both the late cocoon created by the jet in the polar direction and the kilonova powered by the magnetar wind collectively as the ejecta.

In this work, we consider a scenario in which a late jet interacts with ejecta. On this basis, we construct a model of the anisotropic energy injection, including the magnetar wind and jet components. In Section 2.1, the energy output of a magnetar is presented. In Section 2.2, the dynamics of the ejecta are

presented. In Section 2.3, the emission of the ejecta is presented.

2.1. Energy Output of a Magnetar

The simplest form of the energy output for a pulsar can approximate a nearly isotropic or spherical symmetry pulsar wind (Y.-W. Yu et al. 2013; H. Gao et al. 2015; H. Sun et al. 2017). In fact, the available MHD models predict that the maximum energy flux of the pulsar wind is in the equatorial direction (F. C. Michel 1973; S. V. Bogovalov 1999). Although a self-consistent solution to the problem of pulsar wind remains to be found, it is commonly accepted that far away from the pulsar, the wind can be considered as an almost radial supermagnetosonic outflow with purely azimuthal magnetic field and anisotropic angular distribution of the energy flux (F. C. Michel 1982; V. S. Beskin et al. 1998; T. Chiueh et al. 1998; S. Bogovalov & K. Tsinganos 1999). In addition, a jet is generally found around the pulsar (B. D. Metzger et al. 2008; D. Zhang & Z. G. Dai 2010; N. Bucciantini et al. 2012). In a merging event such as GRB 170817A, the jet propagates through the ejecta and forms a cocoon in its path. A late jet responsible for the late engine activity is launched from the central engine and interacts with the redistributed ejecta to form a cocoon. Meanwhile, the later cocoon and other ejecta (kilonova) is heated up by the radioactive decay of the *r*-process elements that are synthesized at the base of the magnetar wind (O. Gottlieb et al. 2018). As long as the jet is inside the ejecta, it deposits most of its energy into the cocoon (O. Gottlieb et al. 2018). Once the late jet's head reaches the outer edge of the ejecta, the shocked jet can get out of the ejecta (late cocoon), i.e., shock breakout occurs (A. Mizuta & K. Ioka 2013; H. Hamidani & K. Ioka 2023b).

In this paper, we define a spherical coordinate (R, θ, φ) with θ being the polar angle and φ being the azimuthal angle, where the coordinate origin is located at the center of the pulsar, R is the distance away from the coordinate origin, and $\theta = 0^\circ$ is along the rotational direction of the pulsar. The powers of the pulsar wind and the jet are taken as $L_{\rm pw}(t, \theta)$ and $L_{\rm jet}(t, \theta)$, respectively. In general, the time-dependent output energy as $\propto(1 + t/t_{\rm sd})^l$ is always used to describe the output energy of a pulsar, where $t_{\rm sd} = 10^2$ s is the spin-down timescale and l is the the decay index. Here, $l = 2$ corresponds to the situation where the magnetic dipole radiation dominates the energy loss of a pulsar. For the pulsar's wind, the angular distribution of the energy flux is generally taken as $\propto\sin^2\theta$ (F. C. Michel 1973; S. V. Bogovalov 1999). Then, the power of the pulsar wind and the jet in unit solid angle can be described as

$$L_{\rm pw}(t, \theta) = \frac{3E_{\rm sd}}{8\pi t_{\rm sd}} f_{\rm iso} \frac{l-1}{(1 + t/t_{\rm sd})^l} \sin^2\theta, \quad (1)$$

$$L_{\rm jet}(t, \theta) = \frac{L_0}{t_{\rm sd}} \frac{l-1}{(1 + t/t_{\rm sd})^l} \exp\left(-\frac{\theta^2}{2\theta_{\rm c}^2}\right), \quad (2)$$

where $f_{\rm iso}$ is the fraction of $E_{\rm sd}$ used to power the pulsar wind, the $\theta_{\rm c}$ is the characteristic angle of the structured jet, $L_0 = (1 - f_{\rm iso})E_{\rm sd} \int_0^{\theta_{\rm jet}}\int_0^{2\pi} \exp[-\theta^2/(2\theta_{\rm c}^2)]d\Omega$, and $\theta_{\rm jet}$ is the opening angle of the jet. Based on Equations (1)–(2), one can have $\int_0^{\infty}\int_{\theta_{\rm jet}}^{\pi-\theta_{\rm jet}}\int_0^{2\pi} L_{\rm pw}(t, \theta)d\Omega dt = f_{\rm iso}E_{\rm sd}$ and $2\int_0^{\infty}\int_0^{\theta_{\rm jet}}\int_0^{2\pi} L_{\rm jet}(t, \theta)d\Omega dt = (1 - f_{\rm iso})E_{\rm sd}$.

2.2. Dynamics of the Ejecta

The dynamics of the ejecta can be obtained based on the evolution of its Lorentz factor $\Gamma_{\rm ej}$, internal energy $E'_{\rm ej,int}$, volume $V'_{\rm ej}$, and radius $R_{\rm ej}$ (D. Kasen & L. Bildsten 2010; Y.-W. Yu et al. 2013; H. Sun et al. 2017; B. Margalit et al. 2018; Y.-F. Li et al. 2024), i.e.,

$$\frac{d\Gamma_{\rm ej}(t, \theta)}{dt} = \frac{\xi_{\rm jet}(t_{\rm b} - t)L_{\rm jet}(t, \theta) + \xi_{\rm pw}L_{\rm pw}(t, \theta) + L_{\rm ra} - L_{\rm ej} - \Gamma_{\rm ej}\mathcal{D}(dE'_{\rm ej,int}/dt')}{M_{\rm ej}c^2 + E'_{\rm ej,int}}, \quad (3)$$

$$\frac{dE'_{\rm ej,int}(t, \theta)}{dt} = [\xi_{\rm jet}(t_{\rm b} - t)L'_{\rm jet}(t, \theta) + \xi_{\rm pw}L'_{\rm pw}(t, \theta) + L'_{\rm ra} - L'_{\rm ej} - p'\frac{dV'_{\rm ej}}{dt'}]\frac{dt'}{dt}, \quad (4)$$

$$\frac{dV'_{\rm ej}}{dt} = 4\pi R_{\rm ej}^2\beta_{\rm ej}c\frac{dt'}{dt}, \quad (5)$$

$$\frac{dR_{\rm ej}}{dt} = \frac{\beta_{\rm ej}c}{1 - \beta_{\rm ej}}, \quad (6)$$

where the parameter measured in the comoving frame of the ejecta is denoted by a prime, $\mathcal{D} = 1/[\Gamma_{\rm ej}(1 - \beta\cos\theta)]$ is the Doppler factor, $L_{\rm ra} = L'_{\rm ra}\mathcal{D}^2$ with $L'_{\rm ra}$ being the radioactive heating rate of the ejecta, $L'_{\rm ej} = L_{\rm ej}/\mathcal{D}^2$ with $L_{\rm ej}$ being the bolometric luminosity of the ejecta, $M_{\rm ej} = 10^{-2}M_\odot$ is the mass of ejecta, $L'_{\rm jet} = L_{\rm jet}/\mathcal{D}^2$, $p' = E'_{\rm ej,int}/(3V'_{\rm ej})$ is the pressure of the gas in the ejecta, $dt'/dt = \mathcal{D}$, and $\beta_{\rm ej} = \sqrt{1 - 1/\Gamma_{\rm ej}^2}$.

Here, we introduce a factor $\xi_{\rm jet}$ with a exponential cutoff at $t_{\rm b}$. $\xi_{\rm jet}$ is defined as the fraction of the jet's energy that is used to accelerate and heat up the ejecta (in the polar direction), and can be estimated as (S. Ai et al. 2024)

$$\xi_{\rm jet} = \begin{cases} 1, & t \leqslant t_{\rm b}, \\ N\exp\left(-\dfrac{t^2}{t_{\rm b}}\right), & t > t_{\rm b}, \end{cases} \quad (7)$$

where $t_{\rm b}$ is the jet breakout time from the ejecta and $N = 0$ is a constant that the efficiency of energy injection after the jet breakout the ejecta.

At the same time, there are important efficiency factors $\xi_{\rm pw}$ that are helpful to calculate engine-fed kilonova (mergernova) emission. The $\xi_{\rm pw}$ is an efficiency parameter to define the fraction of the magnetar's wind energy that is used to accelerate and heat up the ejecta, which could be expressed as

(S. Q. Wang et al. 2015; N. Sarin et al. 2022; S. Ai et al. 2024)

$$\xi_{\rm pw} = 1 - e^{-\tau_\gamma}, \tag{8}$$

where $\tau_\gamma = A_{\rm pw} t^{-2}$ is the optical depth, $A_{\rm pw} = 3\kappa_\gamma M_{\rm ej}/(4\pi\beta_{\rm ej}^2 c^2)$ is the leakage parameter, and κ_γ is the gamma-ray opacity of the ejecta.

For an ejecta formed during the BH/NS–NS merger, the radioactive heating rate of the ejecta $L'_{\rm ra}$ mainly comes from β-decay (Y.-W. Yu & S.-Z. Li 2017), i.e.,

$$L'_{\rm ra} = 2 \times 10^{29} M_{\rm ej} \times \dot{\epsilon}\,(t'), \tag{9}$$

with radioactive power per unit mass (O. Korobkin et al. 2012; J. Barnes et al. 2016; B. D. Metzger 2017)

$$\dot{\epsilon}\,(t') = \epsilon_0 \left[\frac{1}{2} - \frac{1}{\pi}\arctan\left(\frac{t' - t'_0}{t'_\sigma}\right)\right]^\alpha, \tag{10}$$

where $\epsilon_0 = 2 \times 10^{18}\,{\rm erg\,g^{-1}\,s^{-1}}$, $\alpha = 1.3$, $t'_0 = 1.3$ s, and $t'_\sigma = 0.11$ s. The radiative bolometric luminosity can be related to the internal energy of the ejecta as (D. Kasen & L. Bildsten 2010; K. Kotera et al. 2013; Y.-W. Yu et al. 2013)

$$L'_{\rm ej} = \begin{cases} \dfrac{E'_{\rm ej,int}\Gamma_{\rm ej}}{\tau R_{\rm ej}/c}, & t \leqslant t_{\tau=1}, \\ \dfrac{E'_{\rm ej,int}\Gamma_{\rm ej}}{R_{\rm ej}/c}, & t > t_{\tau=1}, \end{cases} \tag{11}$$

where $\tau = \kappa(M_{\rm ej}/V'_{\rm ej})(R_{\rm ej}/\Gamma_{\rm ej})$ is the optical depth of the ejecta, κ is taken in this paper, and the value of $t_{\tau=1}$ is the time at $\tau = 1$.

With a given velocity of the ejecta $\beta_{\rm ej}(t=0)$, the radius of the ejecta $R_{\rm ej}(t=0)$, the volume $V'_{\rm ej} = (4/3)\pi R_{\rm ej}^3(t=0)$, and the ejecta's energy $E'_{\rm ej,int} = (1/2)M_{\rm ej}\beta_{\rm ej}^2 c^2(t=0)$, one can obtain the evolution of $\Gamma_{\rm ej}$, $E'_{\rm ej,int}$, $V'_{\rm ej}$, and $R_{\rm ej}$ with respect to t. Here, we set the launch time of the late jet as $t = 0$.

2.3. Emission of the Ejecta

First, the observed spectrum is nearly blackbody with a typical temperature

$$\varepsilon_{\gamma,p} \approx 4\mathcal{D}k_{\rm B}T' = 4\mathcal{D}k_{\rm B}\left(\frac{E'_{\rm ej,int}(t,\,\theta)}{aV'_{\rm ej}}\right)^{1/4}, \tag{12}$$

where $k_{\rm B}$ is the Boltzmann constant and a is the blackbody radiation constant. For a blackbody spectrum with comoving temperature T', the luminosity at a particular frequency ν is given by (Y.-W. Yu et al. 2013)

$$\nu L_\nu = \frac{1 - e^{-\tau}}{\tau}\frac{8\pi^2\mathcal{D}^2R^2}{h^3c^2}\frac{(h\nu/\mathcal{D})^4}{\exp(h\nu/\mathcal{D}k_{\rm B}T') - 1}. \tag{13}$$

If the radiation field is homogeneous in the ejecta, one can have the bolometric luminosity as $E'_{\rm ej,int}[1 - \exp(-\tau)]/\tau$. Correspondingly, one can have Equation (13) based on Equation (12). If $\tau \gg 1$, the integration over $d\nu$ on the L_ν has $E'_{\rm ej,int}/\tau$. This means that only the fraction of $1/\tau$ in internal energy $E'_{\rm ej,int}$ of the ejecta escapes from the ejecta. If $\tau \ll 1$, the escape fraction of radiation field in the ejecta would be around 1, which is the same as $[1 - \exp(-\tau)]/\tau \sim 1$.

Finally, the ejecta emission surface needs to be accumulated, so a spherical coordinate is introduced into our model (R, θ, φ), with $R = 0$ locating at the burst's central engine and $\theta = 0°$ along the jet's axis. In our calculations, the ejecta moving toward us (along the jet's axis) is divided into 300×200 small patches along the θ and φ directions in their linear space. We assume the observer's location at the direction of $(\theta_{\rm v}, \varphi_{\rm v})$ with $\varphi_{\rm v} = 0°$ and $\theta_{\rm v} \leqslant \pi/2$, so for an off-axis observing angle $\theta_{\rm v}$, the infinitesimal patch of the emission region at (R, θ, φ) makes an angle Θ with respect to the observer, which is given by (A. Kathirgamaraju et al. 2018; X.-Y. Li et al. 2021)

$$\begin{aligned}\cos\Theta &= (\sin\theta\cos\varphi,\ \sin\theta\sin\varphi,\ \cos\theta)\cdot(\sin\theta_{\rm v},\ 0,\ \cos\theta_{\rm v}) \\ &= \sin\theta\cos\varphi\sin\theta_{\rm v} + \cos\theta\cos\theta_{\rm v},\end{aligned} \tag{14}$$

where Θ is the angle between the direction of (θ, φ) and the line of sight, i.e., $(\theta_{\rm v}, \varphi_{\rm v})$ with $\varphi_{\rm v} = 0°$.

Then, the observed time for a photon from the (θ, φ) ejecta can be estimated with (X.-Y. Li et al. 2021)

$$t_{\rm obs}(\theta,\,\varphi,\,\varphi_{\rm v},\,R) = t_{\rm on} + \frac{R_{\rm ej}(1 - \cos\Theta)}{c}, \tag{15}$$

where $t_{\rm on}$ is the arrival time of photons for an observer in the direction of (θ, φ). If the observer is in the direction of $(\theta_{\rm v}, \varphi_{\rm v})$ with $\varphi_{\rm v} = 0°$, the last term should be added. For a given observer time $t_{\rm obs}$, one can obtain the corresponding value of $R_{\rm ej} = R_{\rm obs,ej}(\theta, \varphi, \varphi_{\rm v})$ based on the above equation. Similarly, the optical depth of the ejecta $\tau = \tau_{\rm obs}(\theta, \varphi, \varphi_{\rm v})$, and the blackbody temperature $T' = T_{\rm obs}(\theta, \varphi, \varphi_{\rm v})$ can be obtained. The value of $R_{\rm obs,ej}$, $\tau_{\rm obs}(\theta, \varphi, \varphi_{\rm v})$, $T_{\rm obs}(\theta, \varphi, \varphi_{\rm v})$ is the location of the (θ, φ) ejecta observed at $t_{\rm obs}$ and is used to calculate the observed flux from the (θ, φ) ejecta. The Doppler factor of the (θ, φ) ejecta relative to the observer is

$$\mathcal{D}_{\rm obs}(\theta,\,\varphi,\,\varphi_{\rm v},\,R) = \frac{1}{\Gamma(1 - \beta\cos\Theta)}. \tag{16}$$

The observed total luminosity of the off-axis ejecta is then given by (Y.-W. Yu et al. 2013; G.-L. Wu et al. 2022)

$$\begin{aligned}\nu L_{{\rm obs},\nu}(t_{\rm obs}) = &\frac{1 - e^{-\tau_{\rm obs}}}{\tau_{\rm obs}}\int_0^{\varphi_{\rm m}} d\varphi \int_0^{\theta_{\rm m}} \sin\theta d\theta \\ &\times \frac{8\pi^2\mathcal{D}_{\rm obs}^2 R_{\rm obs,ej}^2}{h^3c^2}\frac{(h\nu/\mathcal{D}_{\rm obs})^4}{\exp(h\nu/\mathcal{D}_{\rm obs}kT_{\rm obs}) - 1}\end{aligned} \tag{17}$$

where h is the Planck constant, the maximum angle $\theta_{\rm m} = \pi/2$, and the maximum angle $\varphi_{\rm m} = 2\pi$.

3. Results: Effects of the Anisotropic Energy Injection on the Ejecta

Energy Injection Efficiency. In previous works studying engine-powered ejecta (kilonova or mergernova; Y.-W. Yu et al. 2013; B. D. Metzger & A. L. Piro 2014; H. Sun et al. 2017; R. T. Wollaeger et al. 2019), the energy injection process is treated through parameterization, e.g., a free parameter $\xi_{\rm pw}$ is adopted to denote the fraction of the magnetar wind energy that is transferred to the ejecta (e.g., take constant parameter $\xi_{\rm pw} = 0.3$ in Y.-W. Yu et al. 2013). Here, we relax this assumption (e.g., Equation (8)) by modeling $\xi_{\rm pw}$ to vary with time and coupled it to the gamma-ray leakage of the ejecta.

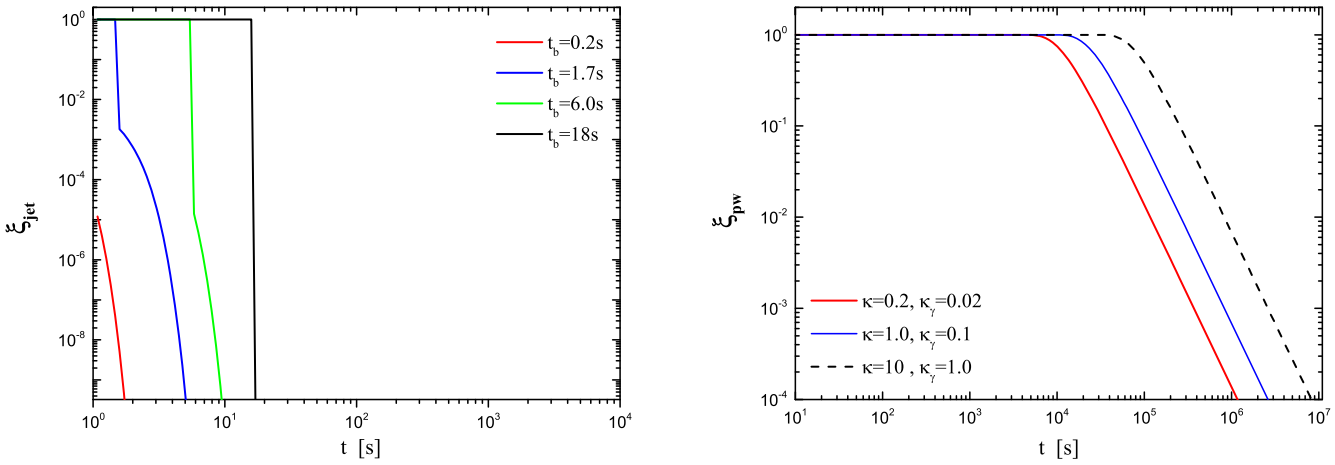

Figure 1. The evolution of the jet energy injecting efficiency ξ_{jet} (left-hand panel) and magnetar wind energy efficiency ξ_{pw} (right-hand panel). In the left-hand panel the solid lines represent the breakout time of the jet at $t_b = 0.2$ s, 1.7 s, 6.0 s, and 18 s corresponding to the red, blue, green, and black solid lines, respectively. In the right-hand panel the solid line represents the magnetar wind energy efficiency at different opacities (lanthanide-free dynamical ejecta) $\kappa = 0.2\ \mathrm{cm^2\ g^{-1}}$ (red line), $1.0\ \mathrm{cm^2\ g^{-1}}$ (blue line), and the black dashed line opacity is $\kappa = 10\ \mathrm{cm^2\ g^{-1}}$ (lanthanide-rich dynamical ejecta, H. Gao et al. 2015).

Recently, S. Ai et al. (2022, 2024) found that effective energy injection occurs mainly before the shock breakout the ejecta; and once the shock breakout through the ejecta, the ξ_{jet} rapidly drops to $\sim$0. Here, we consider the choked jet factor and most of its energy is deposited into the ejecta, with the ξ_{jet} being approximately $\sim$1. Once the shocked jet breakout the ejecta (late cocoon), the ξ_{jet} will undergo a sudden and steep decline, rapidly decaying from $\sim$0.01 to $\sim$0. The time for the shocked jet to breakout through the ejecta depends on a series of complex factors that occur between the final stages of the merger and the launch of the jet. The time delay between the merger of binary NSs and the launch of the jet, as well as the time it takes the jet to breakout the ejecta, are not well constrained by observation considerations, e.g., GRB 170817A, which triggered the Fermi-GBM at $t_{obs} \sim 1.7$ s after the GW170817 signal and lasted for $\sim$2 s. This phenomenon of time delay is a subject of intense debate in the field of GRBs. Although numerical simulations and analytical formulas are commonly used in prediction (D. Lazzati et al. 2010; O. Gottlieb et al. 2018; H. Hamidani & K. Ioka 2021, 2023b), these methods often suffer large uncertainties due to the selection of the physical environment involved and the limited-timescale end of the simulation. Therefore, in this paper, we study several typical breakout time cases (e.g., R. Harrison et al. 2018; H. Hamidani & K. Ioka 2023b; H. Hamidani et al. 2024; V. Mpisketzis et al. 2024) to more precisely understand the effects of jets on the ejecta emission.

Figure 1 shows the relationship of the energy injection efficiency parameters ξ_{pw} and ξ_{jet} with time. The total energy of the engine is $E_{sd} = 10^{52}$ erg, the characteristic angles of structured jets are $\theta_c = 3°$, the radius of the ejecta is $R_{ej}(t = 0) = 3 \times 10^9$ cm, and $\beta_{ej}(t = 0) = 0.35$. The majority of the rotational energy of a magnetar is available as EM radiation $f_{iso} \gtrsim 0.6$ (N. Sarin et al. 2022) and the EM spin energy fraction $f_{iso} = 0.8$. The breakout time of the late jet is $t_b =$ 0.2 s (O. Gottlieb et al. 2018), 1.7 s, 6.0 s, and 18 s (H. Hamidani et al. 2024), corresponding to the red, blue, green, and black lines, respectively. The value of $\kappa \sim 0.1$–$1\ \mathrm{cm^2\ g^{-1}}$,which is lanthanide-poor ejecta (M. M. Kasliwal et al. 2017; V. A. Villar et al. 2017). Here, we select two typical values for the opacity of the ejecta $\kappa = 0.2\ \mathrm{cm^2\ g^{-1}}$ (Y.-W. Yu et al. 2013) and $1\ \mathrm{cm^2\ g^{-1}}$ (V. A. Villar et al. 2017). The gamma-ray opacity of the ejecta $\kappa_\gamma = 0.02\ \mathrm{cm^2\ g^{-1}}$, $0.1\ \mathrm{cm^2\ g^{-1}}$. Our choice of κ_γ is consistent with N. Sarin et al. (2022). In the kilonova context, $1/\beta_{ej} < 5$ and $\kappa_\gamma/\kappa \sim 0.1$ (N. Sarin et al. 2022).

As shown in the left-hand panel of Figure 1, the efficiency of jet energy injection into the ejecta remains at a stable level $\xi_{jet} = 1$ in the initial phase. When the shocked jet breakout, ξ_{jet} will undergo a sudden and steep decline, rapidly decaying $\xi_{jet} \sim 0$. Here, our obtained efficiency results are largely consistent with previous research findings. Specifically, as previously proposed in S. Ai et al. (2022), the heating process proceeds efficiently before the shock successfully breakout from the ejecta. However, once the shock successfully breakout of the ejecta, the heating efficiency rapidly drops to $\sim$0 afterwards. In the right-hand panel of Figure 1, the efficiency of magnetar wind energy injection into the ejecta remains stable during the initial phase. During the initial stage, when the ejecta is in an optically thick state, the magnetar wind is able to continuously and efficiently inject energy into the ejecta. However, once the ejecta becomes optically thin, the injection efficiency of the magnetar wind drops rapidly. Here, our research differs from previous studies (e.g., Y.-W. Yu et al. 2013; B. D. Metzger & A. L. Piro 2014; H. Sun et al. 2017) in that the injection efficiency of the magnetar wind is no longer fixed, but is expressed by the parameter ξ_{pw}, which changes with time. However, the introduction of the factor of the effective optical depth for gamma-rays κ_γ has not had a significant impact on our research results.

Anisotropic and Isotropic Energy Injection of the Central Engine. In the left-hand panel of Figure 2, we present the multband light curve of the emission from the ejecta with anisotropic energy injection (along the jet's axis direction, viewing angles $\theta_v = 0°$). These light curves include X-ray band (1 keV), *U*-band (30 eV), and optical band (1 eV), and are represented by solid lines of different colors, each corresponding to a different jet breakout time from the ejecta (the magenta lines for $t_b = 1.7$ s, the red lines for $t_b = 6.0$ s, and the black lines for $t_b = 18$ s). Here, the characteristic angles of structured jets is $\theta_c = 3°$, the engine lifetime is $t_{sd} = 10^2$ s (B. Margalit et al. 2018), and the total energy of the engine is $E_{sd} = 10^{52}$ erg. The ejection uses a typical lanthanum-poor ejecta with a parameter $\kappa = 1\ \mathrm{cm^2\ g^{-1}}$ and $\kappa_\gamma = 0.1\ \mathrm{cm^2\ g^{-1}}$

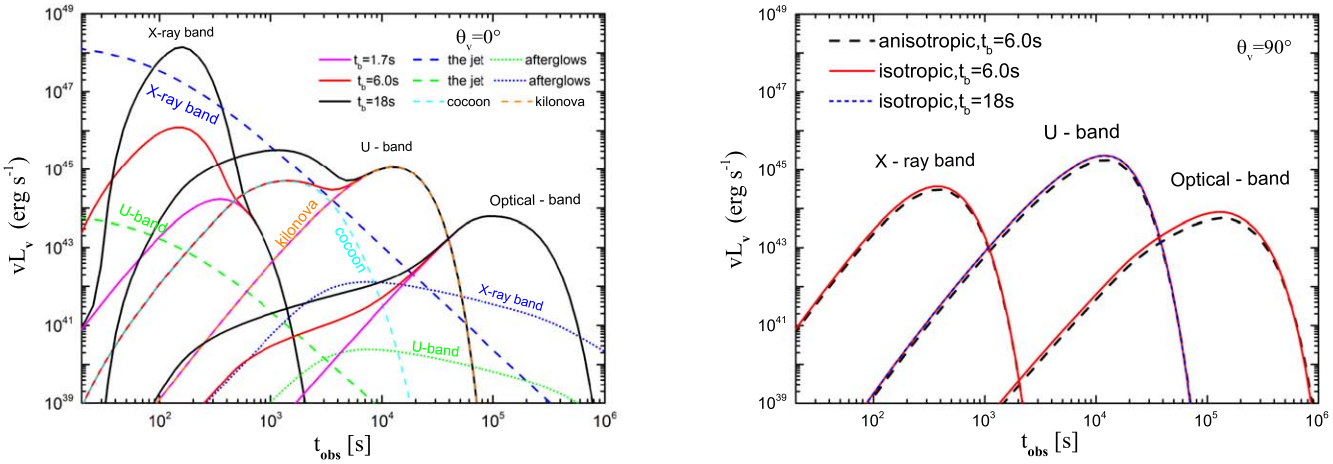

Figure 2. The multband light curve of the emission from the ejecta with anisotropic energy injection, including 1 keV (X-ray band), 30 eV (*U*-band), and 1 eV (optical band). The left-hand panel shows the light curves of the ejecta, which are represented by solid lines of different colors (along the jet's axis direction, $\theta_v = 0°$), each corresponding to a different jet breakout time from the ejecta (the magenta lines for $t_b = 1.7$ s, the red lines for $t_b = 6$ s, and the black lines for $t_b = 18$ s). The blue (X-ray band) and green (*U*-band) dashed lines represent the emission of from the Poynting-flux-dominated jet (D. Xiao & Z.-G. Dai 2017; D. Xiao et al. 2019), the blue (X-ray band) and green (*U*-band) dotted lines represent the light curve of the emission of afterglows in GRB 170817A (J. Ren et al. 2020). The right-hand panel shows the multband light curve of the emission from the ejecta with anisotropic (the black dashed lines) and isotropic (the red solid lines) energy injection (along the equatorial direction, viewing angles $\theta_v = 90°$). The blue dotted line represents the emission light curve of the ejecta at breakout time $t_b = 18$ s.

(B. D. Metzger 2019), the other relevant parameters are consistent with Figure 1.

In the left-hand panel of Figure 2, it can be seen that for an observer in the jet's axis direction, when the shocked jet breakout time is relatively short ($t_b = 1.7$ s), the energy injection efficiency of the jet is very low, almost negligible. This finding is consistent with the energy injection efficiency results depicted in left-hand panel of Figure 1. The shocked jet breakout the ejecta so quickly that the actual energy injection is extremely brief and then quickly decays to ∼0. Therefore, in this case, the light curve of the ejecta (magenta solid line) does not show a significant difference from the results of previous researchers (e.g., not considering the contribution of the jet in Y.-W. Yu et al. 2013). However, as the jet breakout time increases, the actual energy injection efficiency of the jet also increases accordingly. At this time, the light curves of the ejecta (the red and black solid lines) rise more steeply in the early stages and even display a significant bump feature, particularly in the *U*-band ($\sim 10^2$–10^3 s). This feature is due to the contribution of the cocoon formed by the interaction of the jet with the ejecta (the cyan dashed line in the figure), resulting in this change in the light curve.

Furthermore, the left-hand panel Figure 2 also shows the light curves of the Poynting-flux-dominated jet emission (D. Xiao & Z.-G. Dai 2017; D. Xiao et al. 2019), where the X-ray band is represented by a blue dashed line and the *U*-band is represented by a green dashed line. Additionally, this figure includes the light curve of the GRB 170817A afterglow emission (J. Ren et al. 2020), where the afterglow in the X-ray band is denoted by a blue dotted line and the afterglow in the *U*-band is denoted by a green dotted line. Notably, in the *U*-band section, this figure additionally presents the light curves of two components: the cocoon and the kilonova emissions, which are, respectively, represented by cyan and orange dashed lines. In the X-ray band, the emission of the Poynting-flux-dominated jet is indeed about one to two orders of magnitude higher than the emission from the ejecta with anisotropic energy injection. This significant difference is mainly due to whether the shocked jet can rapidly breakout the ejecta. In the case of binary NS mergers, the time for the jet to breakout the ejecta is usually short, often lasting only a few seconds or even less, which greatly limits the deposition time of energy in the ejecta. Therefore, it is a challenging task to detect the emission effects of magnetar anisotropic energy injection during a binary NS merger event at X-ray band. In the *U*-band and optical band, the emission from the Poynting-flux-dominated jet does not significantly exceed the ejecta emission with anisotropic energy injection during $\sim 10^2$–10^3 s. However, more notably, the significant bump feature induced by anisotropic energy injection can be clearly observed in the *U*-band, which provides an excellent observation opportunity to study the anisotropic energy injection of a magnetar.

In the right-hand panel of Figure 2, we present the multband light curve of the emission from the ejecta with anisotropic (the black dashed lines) and isotropic (the red solid lines) energy injection (along the equatorial direction, viewing angles $\theta_v = 90°$). In this figure, it is clearly shown that in the equatorial direction the two energy injection methods have hardly any significant effect on the light curves of the ejecta's emission. An interesting phenomenon is that the light curve of the ejecta's emission at the jet breakout time of $t_b = 6.0$ s almost overlaps with the light curve at $t_b = 18$ s (blue dotted line). This indicates that under off-axis observations, the effect of jet breakout time on the ejecta's emission becomes negligible. This finding is consistent with previous studies of a kilonova driven by magnetar wind, further confirming that the ejecta's emission in the equatorial direction is primarily driven by magnetar wind. In the jet's axis direction, the emission of the ejecta is primarily affected by the jet.

The Effect of the Characteristic Angle and Energy Distribution Ratio. In the left-hand panel of Figure 3, we investigated the effect of the characteristic angle θ_c on the emission light curves of the ejecta, where the EM spin energy fraction is $f_{iso} = 0.8$, the breakout time of the jet is $t_b = 6.0$ s, and the other parameters are the same as Figure 1, From this figure, as the characteristic angle θ_c gradually decreases (the blue solid line $\theta_c = 5°$, the green solid line $\theta_c = 3°$, the red solid line $\theta_c = 1°$), the relativistic beaming effect of the jet gradually is strong.

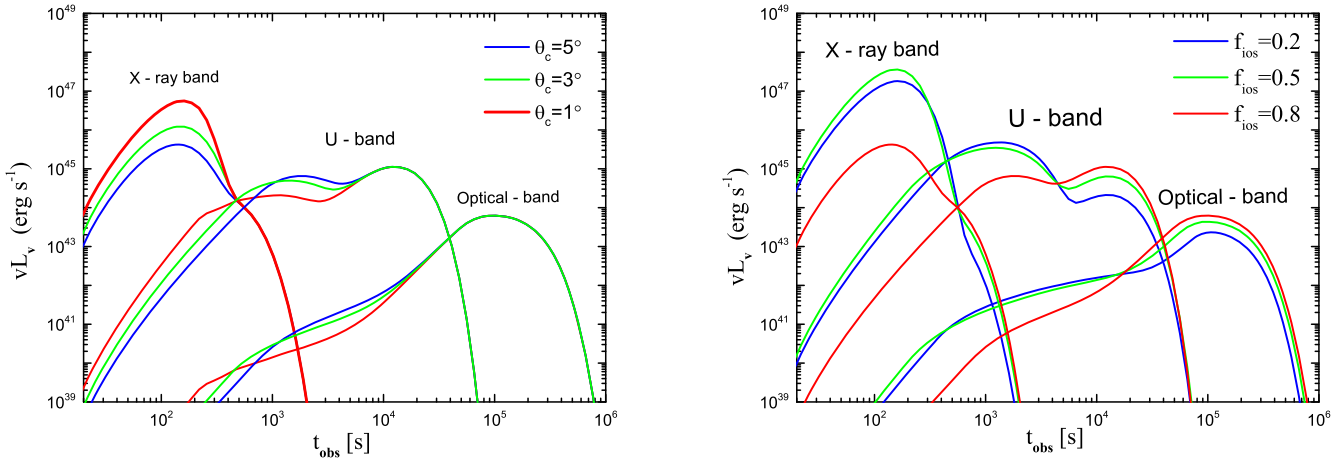

Figure 3. The left-hand panel shows the effect of the characteristic angle θ_c of the structured jet on the emission light curves of the ejecta. The distributions of the blue solid line, green solid line, and red solid line correspond to the characteristic angle $\theta_c = 5°, 3°, 1°$ of the structured jet. The right-hand panel shows the effect of the energy distribution ratio of magnetar f_{iso} on the emission light curves of the ejecta. The distributions of the blue solid line, green solid line, and red solid line correspond to the EM spin energy fraction is $f_{iso} = 0.2,\ 0.5,\ 0.8$.

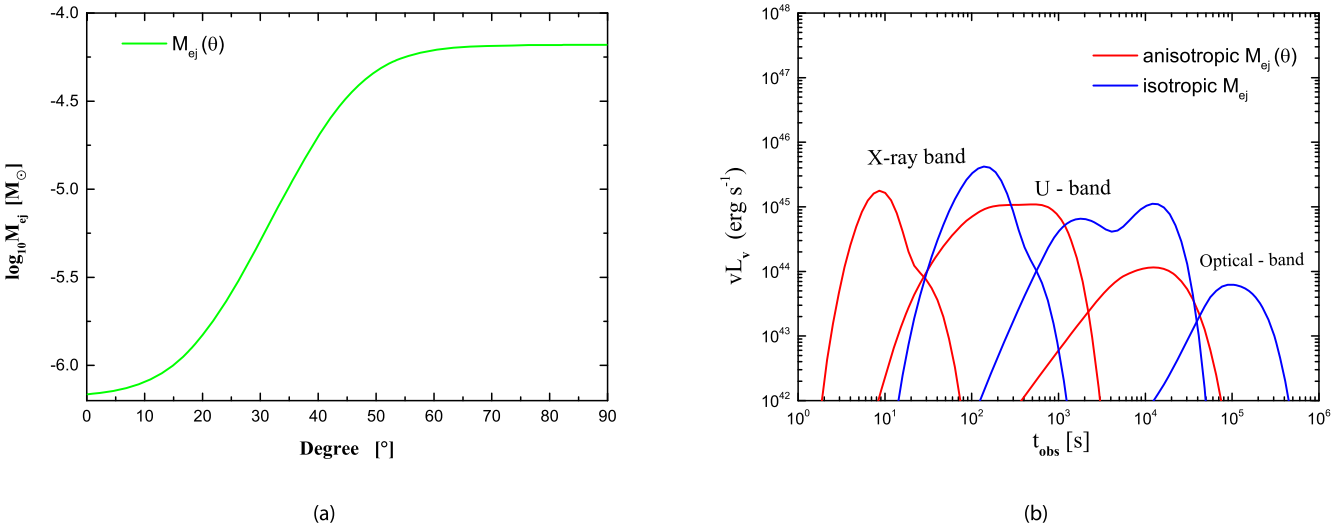

Figure 4. Panel (a): the distribution of mass of ejecta with angle θ. Panel (b): the multband light curve of the emission from the ejecta with anisotropic (the red line) and isotropic (the blue line) merger ejecta, including 1 keV (X-ray band), 30 eV (U-band), and 1 eV (optical band).

Accordingly, the bump or rising effect in the emission light curve of the ejecta also becomes increasingly significant. Especially when the characteristic angle decreases to $\theta_c = 1°$, the bump or rising effect in the light curve is most significant.

In the right-hand panel of Figure 3, we investigate the effect of different proportions of f_{iso} (i.e., magnetar wind and structural jets driven by the central engine magnetar) on the ejecta emissions, where the characteristic angle is $\theta_c = 5°$, the breakout time of the jet is $t_b = 6.0$ s, the other parameters are the same as Figure 1, and the blue, green, and red solid line distributions correspond to the EM spin energy fraction, which is $f_{iso} = 0.2,\ 0.5,\ 0.8$. In this figure it can be seen that when f_{iso} is high, the bump or rise effect on the light curve caused by anisotropic energy injection becomes relatively insignificant. However, when f_{iso} is low, the effect is more significant. Specifically, as the proportion of jet energy increases, the contribution of jet to the ejecta increases correspondingly, resulting in a more obvious bump effect. In the U-band, the blue solid line shows that the peak luminosity of the early bump is obviously higher than that of the kilonova. The red solid line shows that the early peak luminosity of the bump is lower than the peak luminosity of the kilonova. This comparison clearly demonstrates the effect of different f_{iso} on the characteristics of the ejecta's emission.

Anisotropic and Isotropic Ejecta. In Figure 4, we also provide the multband light curves of the emission from the ejecta with anisotropic (the red line) and isotropic (the blue line) merger ejecta, including 1 keV (X-ray band), 30 eV (U-band), and 1 eV (optical band). We adopted the expression of G.-L. Wu et al. (2022) about the angular distribution of the mass of the ejecta and provide this distribution curve in panel (a) of Figure 4. In panel (a), we can see that the mass distribution of the ejecta in the jet's axis direction is lesser, while most of the mass is concentrated near the equatorial direction. This distribution property is reflected in the light curve of panel (b). In the anisotropic energy injection model we can also see that the light curves of anisotropic ejecta rise significantly faster in the early stages compared to the isotropic ejecta. This is due to the majority of the mass being distributed in the equatorial region, resulting in the low-mass ejecta in the polar region becoming optically thin earlier and thus reaching the emission peak luminosity sooner. Moreover, we found that

the light curves of anisotropic ejecta in the U-band exhibit a similar brief plateau. This happens because under the same jet energy injection condition the mass distribution of the ejecta in the jet's axis direction is relatively small, which leads to the rapid rise of the early peak. Furthermore, we also find that in the case of anisotropic energy injection, the anisotropic ejecta does not exhibit a distinct early bump. This finding suggests that if a jet exists in the system, a bump from the cocoon (i.e., the ejecta powered by the jet) could only appear in the optical/U-band light curve for a quasi-isotropic ejecta. In future observations, the early optical/U-band observations could be useful in distinguishing the evolution patterns of the cocoon.

4. Summary and Discussions

This paper is based on the scenario in which a late jet interacts with ejecta, we present a model of the anisotropic energy injection from a magnetar central engine, considering both the magnetar wind and the jet component. and investigate its effect on the emission of the ejecta. We found that (1) for observers located in the equatorial direction there is no significant difference in the light curves obtained from our injection model compared to previous isotropic energy injection models. (2) For observers situated along the jet's axis our model exhibits a steeper rise in the early stages of the U-band and optical band, even forming a bump (cocoon formed by jet powered ejecta). This suggests that the anisotropic "magnetar wind and jet" model may have unique radiation features when observed along the jet's axis.

In addition, by comparing the afterglow emission of GRB 170817A (J. Ren et al. 2020) in Figure 2, it can be clearly found that the bump characteristics caused by anisotropic energy injection can be clearly seen in the UV-band and optical band. As shown in Figure 3, by comparing the light curves at different characteristic angles θ_c, we have found that as the characteristic angle decreases, the bump or rise effect of the light curve becomes more significant. Furthermore, we have also investigated the effect of the energy distribution ratio of magnetar $f_{\rm iso}$ on the emission of the ejecta. When $f_{\rm iso}$ is higher, indicating that the magnetar's wind dominates, the effect of anisotropic energy injection on the emission of the ejecta becomes relatively insignificant. Conversely, when $f_{\rm iso}$ is lower, the contribution of the jet to the ejecta increases, resulting in more significant features on the light curve. This clearly demonstrates the effect of $f_{\rm iso}$ on the radiation of the ejecta. In Figure 4, we find that under the condition of anisotropic energy injection, the emission from anisotropic ejecta appears earlier and reaches the peak of the light curve sooner compared to isotropic ejecta. In the future, as some detailed observations can be achieved (e.g., by the Einstein Probe W. Yuan 2022), we can even use the emission light curve to probe the outline structure of the merger ejecta.

It should be noted that energy injection efficiency $\xi_{\rm pw}$ is a key parameter, while in previous models $\xi_{\rm pw}$ was assumed to be a constant. Here, we relax this assumption, modeling $\xi_{\rm pw}$ to vary with time. However, the introduction of the factor of the effective optical depth for gamma-rays κ_γ has not had a significant impact on our research results. In Figure 1, we also show the opacity $\kappa = 10\,{\rm cm^2\,g^{-1}}$ for a lanthanide-rich dynamic ejecta. For the jet energy injection efficiency $\xi_{\rm jet}$, our results are generally consistent with previous studies (S. Ai et al. 2022). However, the difference is that we consider the effect of the shocked jet breakout time $t_{\rm b}$ from the ejecta. The $t_{\rm b}$ is determined by a series of complex events occurring between the final stages of the merger and the jet launch, and there is considerable uncertainty in existing research regarding the determination of $t_{\rm b}$. We use these efficiency parameters in our calculations, but we lack a deep understanding of the physical processes behind them. Therefore, future studies need to explore these physical processes in more detail in order to more accurately describe the energy injection and heating mechanisms of engine driven kilonova.

Furthermore, it is crucial to emphasize that the effect of anisotropic energy injection cannot be observed even within the jet's axis for a low energy output central engine. At the same time, we do not discuss power-law structured jets because there is no significant difference between power-law structured jet and Gaussian structured jet on the light curve features of the ejecta, which will not affect the results of this paper.

Our results reveal that the anisotropic energy output of the magnetar wind and the jet component should be well considered in modeling the ejecta emission by considering the energy injection from a magnetar. With the improvement of the observation accuracy of the detection instruments, these radiation characteristics may reveal more details about the energy injection from the magnetar.

Acknowledgments

This work is supported by the National Natural Science Foundation of China (grant Nos. 12273005 and 12133003), the special funding for Guangxi Bagui Scholars, China Manned Spaced Project (CMS-CSST-2021-B11), and the special funding for Guangxi Bagui Scholars, the Guangxi Talent Program ("Highland of Innovation Talents").

ORCID iDs

Yu-Fei Li https://orcid.org/0009-0006-2841-678X

References

Abbott, B. P., Abbott, R., Abbott, T. D., et al. 2017a, ApJL, 848, L13
Abbott, B. P., Abbott, R., Abbott, T. D., et al. 2017b, PhRvL, 119, 161101
Ai, S., Gao, H., & Zhang, B. 2024, arXiv:2405.00638
Ai, S., Zhang, B., & Zhu, Z. 2022, MNRAS, 516, 2614
Barnes, J., Kasen, D., Wu, M.-R., & Martínez-Pinedo, G. 2016, ApJ, 829, 110
Beskin, V. S., Kuznetsova, I. V., & Rafikov, R. R. 1998, MNRAS, 299, 341
Bogovalov, S., & Tsinganos, K. 1999, MNRAS, 305, 211
Bogovalov, S. V. 1999, A&A, 349, 1017
Bogovalov, S. V., & Khangoulian, D. V. 2002, MNRAS, 336, L53
Bromberg, O., Nakar, E., Piran, T., & Sari, R. 2011, ApJ, 740, 100
Bucciantini, N., Metzger, B. D., Thompson, T. A., & Quataert, E. 2012, MNRAS, 419, 1537
Burrows, D. N., Grupe, D., Capalbi, M., et al. 2006, ApJ, 653, 468
Chiueh, T., Li, Z.-Y., & Begelman, M. C. 1998, ApJ, 505, 835
Churazov, E. M., Khabibullin, I. I., & Bykov, A. M. 2024, A&A, 688, A4
Dai, Z. G., & Lu, T. 1998, A&A, 333, L87
De Pasquale, M., Schady, P., Kuin, N. P. M., et al. 2010, ApJL, 709, L146
Fan, Y.-Z., Yu, Y.-W., Xu, D., et al. 2013, ApJL, 779, L25
Fong, W., Berger, E., Chornock, R., et al. 2013, ApJ, 769, 56
Fox, D. B., Frail, D. A., Price, P. A., et al. 2005, Natur, 437, 845
Fujibayashi, S., Wanajo, S., Kiuchi, K., et al. 2020, ApJ, 901, 122
Gaensler, B. M., Arons, J., Kaspi, V. M., et al. 2002, ApJ, 569, 878
Gaensler, B. M., Pivovaroff, M. J., & Garmire, G. P. 2001, ApJL, 556, L107
Gao, H., Ding, X., Wu, X.-F., Dai, Z.-G., & Zhang, B. 2015, ApJ, 807, 163
Gao, H., Zhang, B., Lü, H.-J., & Li, Y. 2017, ApJ, 837, 50
Gehrels, N., & Sarazin, C. L. 2005, Natur, 437, 851
Goldstein, A., Veres, P., Burns, E., et al. 2017, ApJL, 848, L14
Gottlieb, O., Metzger, B. D., Quataert, E., et al. 2023, ApJL, 958, L33
Gottlieb, O., Nakar, E., & Piran, T. 2018, MNRAS, 473, 576

Hamidani, H., & Ioka, K. 2021, MNRAS, 500, 627
Hamidani, H., & Ioka, K. 2023a, MNRAS, 520, 1111
Hamidani, H., & Ioka, K. 2023b, MNRAS, 524, 4841
Hamidani, H., Kimura, S. S., Tanaka, M., & Ioka, K. 2024, ApJ, 963, 137
Harrison, R., Gottlieb, O., & Nakar, E. 2018, MNRAS, 477, 2128
Helfand, D. J., Gotthelf, E. V., & Halpern, J. P. 2001, ApJ, 556, 380
Hester, J. J., Mori, K., Burrows, D., et al. 2002, ApJL, 577, L49
Hester, J. J., Scowen, P. A., Sankrit, R., et al. 1995, ApJ, 448, 240
Hotokezaka, K., Kiuchi, K., Kyutoku, K., et al. 2013, PhRvD, 87, 024001
Ioka, K., Kobayashi, S., & Zhang, B. 2005, ApJ, 631, 429
Kasen, D., & Bildsten, L. 2010, ApJ, 717, 245
Kasliwal, M. M., Nakar, E., Singer, L. P., et al. 2017, Sci, 358, 1559
Kathirgamaraju, A., Barniol Duran, R., & Giannios, D. 2018, MNRAS, 473, L121
Kisaka, S., & Ioka, K. 2015, ApJL, 804, L16
Komissarov, S. S., & Lyubarsky, Y. E. 2003, MNRAS, 344, L93
Korobkin, O., Rosswog, S., Arcones, A., & Winteler, C. 2012, MNRAS, 426, 1940
Kotera, K., Phinney, E. S., & Olinto, A. V. 2013, MNRAS, 432, 3228
Lazzati, D., Morsony, B. J., & Begelman, M. C. 2010, ApJ, 717, 239
Li, S.-Z., Liu, L.-D., Yu, Y.-W., & Zhang, B. 2018, ApJL, 861, L12
Li, X.-Y., Lin, D.-B., Ren, J., et al. 2021, ApJ, 922, 22
Li, Y.-F., Lin, D.-B., Ren, J., et al. 2024, ApJ, 960, 17
Liang, E.-W., Zhang, B.-B., & Zhang, B. 2007, ApJ, 670, 565
Lu, F. J., Wang, Q. D., Aschenbach, B., Durouchoux, P., & Song, L. M. 2002, ApJL, 568, L49
Lyubarsky, Y. E. 2002, MNRAS, 329, L34
Margalit, B., Metzger, B. D., Thompson, T. A., Nicholl, M., & Sukhbold, T. 2018, MNRAS, 475, 2659
Matsumoto, T., Ioka, K., Kisaka, S., & Nakar, E. 2018, ApJ, 861, 55
Metzger, B. D. 2017, LRR, 20, 3
Metzger, B. D. 2019, LRR, 23, 1
Metzger, B. D., & Berger, E. 2012, ApJ, 746, 48
Metzger, B. D., & Piro, A. L. 2014, MNRAS, 439, 3916
Metzger, B. D., Quataert, E., & Thompson, T. A. 2008, MNRAS, 385, 1455
Metzger, B. D., Thompson, T. A., & Quataert, E. 2018, ApJ, 856, 101
Michel, F. C. 1973, ApJL, 180, L133
Michel, F. C. 1982, RvMP, 54, 1
Mizuta, A., & Ioka, K. 2013, ApJ, 777, 162
Mpisketzis, V., Duqué, R., Nathanail, A., Cruz-Osorio, A., & Rezzolla, L. 2024, MNRAS, 527, 9159
Nakar, E., & Piran, T. 2017, ApJ, 834, 28
Nousek, J. A., Kouveliotou, C., Grupe, D., et al. 2006, ApJ, 642, 389
Panaitescu, A., Mészáros, P., Gehrels, N., Burrows, D., & Nousek, J. 2006, MNRAS, 366, 1357
Pavlov, G. G., Kargaltsev, O. Y., Sanwal, D., & Garmire, G. P. 2001, ApJL, 554, L189
Radice, D., Perego, A., Hotokezaka, K., et al. 2018, ApJ, 869, 130
Rastinejad, J. C., Gompertz, B. P., Levan, A. J., et al. 2022, Natur, 612, 223
Ren, J., Lin, D.-B., Zhang, L.-L., et al. 2020, ApJL, 901, L26
Ruderman, M. 1975, NYASA, 262, 164
Sari, R., Piran, T., & Narayan, R. 1998, ApJL, 497, L17
Sarin, N., Omand, C. M. B., Margalit, B., & Jones, D. I. 2022, MNRAS, 516, 4949
Savchenko, V., Ferrigno, C., Kuulkers, E., et al. 2017, ApJL, 848, L15
Shibata, M. 1999, PhRvD, 60, 104052
Sun, H., Zhang, B., & Gao, H. 2017, ApJ, 835, 7
Troja, E., Cusumano, G., O'Brien, P. T., et al. 2007, ApJ, 665, 599
Troja, E., Fryer, C. L., O'Connor, B., et al. 2022, Natur, 612, 228
Villar, V. A., Guillochon, J., Berger, E., et al. 2017, ApJL, 851, L21
Virgili, F. J., Zhang, B., O'Brien, P., & Troja, E. 2011, ApJ, 727, 109
Wang, S. Q., Wang, L. J., Dai, Z. G., & Wu, X. F. 2015, ApJ, 807, 147
Wang, Y., Zhang, B., & Zhu, Z. 2024, MNRAS, 528, 3705
Weisskopf, M. C., Hester, J. J., Tennant, A. F., et al. 2000, ApJL, 536, L81
Wollaeger, R. T., Fryer, C. L., Fontes, C. J., et al. 2019, ApJ, 880, 22
Wu, G.-L., Yu, Y.-W., & Li, S.-Z. 2022, Univ, 8, 633
Xiao, D., & Dai, Z.-G. 2017, ApJ, 846, 130
Xiao, D., Zhang, B.-B., & Dai, Z.-G. 2019, ApJL, 879, L7
Yang, J., Ai, S., Zhang, B.-B., et al. 2022, Natur, 612, 232
Yu, Y.-W., & Li, S.-Z. 2017, MNRAS, 470, 197
Yu, Y.-W., Liu, L.-D., & Dai, Z.-G. 2018, ApJ, 861, 114
Yu, Y.-W., Zhang, B., & Gao, H. 2013, ApJL, 776, L40
Yuan, W. 2022, in 44th COSPAR Scientific Assembly (Athens: COSPAR), 1966
Zhang, B. 2013, ApJL, 763, L22
Zhang, B., Fan, Y. Z., Dyks, J., et al. 2006, ApJ, 642, 354
Zhang, B., & Mészáros, P. 2001, ApJL, 552, L35
Zhang, D., & Dai, Z. G. 2010, ApJ, 718, 841